

Thin accretion disk and shadow of Kerr-Sen black hole in Einstein-Maxwell-dilaton-axion gravity

Haiyuan Feng ^{a,1,†} Rong-Jia Yang ^{c,2,§} and Wei-Qiang Chen ^{e1,**}

¹*Department of Physics, Southern University of Science and Technology,
Shenzhen 518055, Guangdong, China*

²*College of Physical Science and Technology,
Hebei University, Baoding 071002, China*

Abstract

We investigate the accretion process in a thin disk surrounding a supermassive black hole in Einstein-Maxwell-dilaton-axion (EMDA) gravity by using the Novikov-Thorne model. The results reveal that as the dilaton parameter r_2 increase, the energy flux, radiation temperature, spectra luminosity, and radiative efficiency of the disk all increases. By narrowing down the dilaton parameter range to $0 \leq \frac{r_2}{M} \leq 0.4$, we discover that in the high-frequency region, the Kerr-Sen black hole demonstrates higher energy output compared to the Kerr black hole. We also investigated the Kerr-Sen black hole shadow in a uniform plasma environment. For a fixed inclination angle of $\theta_0 = 90^\circ$, $\frac{r_2}{M} = \frac{a}{M} = 0.5$, the shadow increase as the homogeneous plasma parameter k increase. Conversely, when $k = 0.1$ and $\frac{a}{M} = 0.5$, an increase in r_2 leads to a decrease in the shadow. Furthermore, by using observational data from M87* and Sgr A*, we compared the theoretical and observed shadow diameters to constrain the range of the model parameters.

^a Corresponding author

^c Corresponding author

^e Corresponding author

[†] Email address: fenghaiyuanphysics@gmail.com

[§] Email address: yangrongjia@tsinghua.org.cn

^{**} Email address: chenwq@sustech.edu.cn

I. INTRODUCTION

The black holes predicted by the theory of general relativity (GR) are intriguing celestial entities. They emerge as the most potent sources of gravitational fields in the cosmology, with anticipated characteristics of exceedingly elevated spin and magnetic intensity. Their distinct attributes render black holes an optimal setting for investigating both material properties and gravitational effects within the realm of astrophysical experiments. In recent years, there has been a significant increase in observational evidence supporting the existence of black holes. A significant breakthrough in the field of black hole research was achieved with the detection of gravitational waves resulting from the merger of a binary black hole system, a discovery made possible by the collaborative efforts of the LIGO and Virgo teams [1]. Another remarkable milestone was the unveiling of the first image capturing the shadow of the M87* black hole [2, 3]. More recently, the Event Horizon Telescope (EHT) utilized Very Long Baseline Interferometry to capture an image of the supermassive black hole at the center of our galaxy, Sgr A*[4]. Furthermore, the presence of black holes can be confirmed through the observed electromagnetic spectrum of accretion disks [5–7]. These recent achievements provide valuable insights into our understanding the characteristics of accretion disks surrounding supermassive compact objects near the event horizon.

It is widely accepted that compact objects such as black holes gain their mass through the accretion process. Additionally, the presence of an accretion disk is a critical factor in sustaining a high accretion rate around these compact objects. An accretion disk is a structure that forms around a central compact object, such as a black hole, neutron star, or white dwarf. It is composed of diffuse material, such as gas and dust, which slowly spirals inward towards the central object due to gravitational forces. As the material spirals inward, it releases gravitational energy in the form of radiation, which can be observed and analyzed by astronomers. In addition, images of accretion disks surrounding black holes have been a subject of intense research in observational astronomy, as they provide valuable information about the properties of these compact objects and the processes occurring in their vicinity. The standard model of geometrically thin and optically thick accretion disks was first proposed by Shakura and Sunyaev, and later generalized by Page, Novikov, and Thorne to include GR [8–11]. They assumed that the accretion disk is in a steady-state, meaning that the mass accretion rate \dot{M} was constant and did not depend on the radius

of the disk. At the same time, the disk was also assumed to be in hydrodynamic and thermodynamic equilibrium, which ensured a black body electromagnetic spectrum and properties of emitted radiation. This model has been successful in explaining the observed spectral features of astrophysical black holes.

On the other hand, the study of black hole shadow in a plasma environment is an emerging field that bridges the gap between astrophysics and GR, providing a richer understanding of both black holes and the interstellar medium. This plasma not only influences light trajectories through the gravitational effects of compact objects but also acts as a dispersive medium [2, 12]. Therefore, it is reasonable to assume that black holes and other exotic compact objects are surrounded by plasma in realistic astrophysical environments. Consequently, studying the observable effects of black hole shadows within plasma becomes an intriguing and valuable approach. Investigating these effects allows us to probe the interactions between radiation and plasma in the vicinity of black holes, offering insights into the properties of the plasma, such as its density and distribution. Moreover, this research helps in refining the theoretical models of black hole physics, as the plasma's influence must be accounted for in precise measurements of black hole parameters. As observational techniques advance, particularly with high-resolution instruments like the EHT, understanding the role of plasma becomes increasingly crucial for accurate interpretation of black hole shadow, ultimately contributing to our knowledge of the universe's most extreme environments.

The discernible features present in the emission spectra of accretion disks and the observation of the black hole shadow provide valuable insights into the characteristics of the central massive object. Furthermore, these observations serve as a testing ground for modified theories. Extensive research has been investigated on the characteristics of thin disks and black shadow in diverse background spacetimes [13–53]. Among many alternative theories, the Einstein-Maxwell-dilaton-axion (EMDA) model [54, 55] has attracted significant attention, for example, the accretion onto this black hole has been discussed in Ref.[56]. In this model, the dilaton field and the pseudoscalar axion are integrated, both of which are intricately linked to the metric and the Maxwell field. The origins of the dilaton and axion fields can be traced back to string compactifications, presenting compelling implications for inflationary and late-time accelerated cosmologies [57, 58]. As a result, we will focus on the influence of theoretical parameters on the properties of the thin accretion disk and shadow in the EMDA model.

Moreover, the dilaton parameter $r_2 \equiv \frac{Q^2}{M}$ has been constrained through observations in EMDA theory. For example, a preferred value of $r_2 \approx 0.2M$ is determined based on the optical continuum spectrum of quasars [59]. Additionally, recent investigations have imposed observational constraints on the parameter ($0.1M \lesssim r_2 \lesssim 0.4M$) [60]. Finally, a constraint on the r_2 is obtained by employing simulated data replicating potential observations of the S2 star via a gravity interferometer [61]. This demonstrated that enhanced astrometric accuracy can effectively narrow down the acceptable range of the dilaton parameter to $r_2 \lesssim 0.066M$.

The article is organized as follows: In Sec.II, the EMDA model and the Kerr-Sen black hole will be briefly reviewed. In Sec.III, we will present the geodesic equation governing the motion of timelike particles moving in the equatorial plane. We will plot the variations of particle's specific angular momentum \tilde{L} , specific energy \tilde{E} , angular velocity Ω , and the innermost stable circular orbit r_{ISCO} with respect to the dilaton parameter r_2 . We will investigate the physical characteristics of thin accretion disk surrounding Kerr-Sen black hole, with a particular focus on the influence of the dilaton parameter on the energy flux, temperature, and emission spectrum of the accretion process. In Sec.IV, our main objective is to study the shadow of black hole within a uniform plasma environment. Additionally, we will constrain the range of these parameters using data from M87* and Sgr A*. Finally, Sec.V addresses conclusions and discussions. For convenience, we will use signature convention $(-, +, +, +)$ for the spacetime metric throughout the article.

II. KERR-SEN BLACK HOLE IN EINSTEIN-MAXWELL-DILATON-AXION GRAVITY

The EMDA model is derived from the low-energy limit behavior of heterotic string theory. It is composed of the dilaton field χ , a gauge vector field A_μ , the metric $g_{\mu\nu}$, and a pseudo-scalar axion field ξ [54, 55, 62]. The action of the EMDA model can be formulated through the coupling of supergravity and super-Yang Mills theory, and it can be described by the

$$S = \frac{1}{16\pi} \int \sqrt{-g} d^4x \left[R - 2\partial_\mu \chi \partial^\mu \chi - \frac{1}{2} e^{4\chi} \partial_\mu \xi \partial^\mu \xi + e^{-2\chi} f_{\mu\nu} f^{\mu\nu} + \xi f_{\mu\nu} \tilde{f}^{\mu\nu} \right], \quad (1)$$

Where R represents the Ricci scalar and $f_{\mu\nu}$ denotes the second-order antisymmetric Maxwell field strength tensor, given by $f_{\mu\nu} = \nabla_\mu A_\nu - \nabla_\nu A_\mu$, while $\tilde{f}^{\mu\nu}$ signifies the dual tensor of

the field strength. The variation of these four fields leads to the following motion equations

$$\left\{ \begin{array}{l} \square\chi - \frac{1}{2}e^{4\chi}\nabla_{\mu}\xi\nabla^{\mu}\xi + \frac{1}{2}e^{-2\chi}f_{\mu\nu}f^{\mu\nu} = 0 \\ \square\xi + 4\nabla_{\mu}\xi\nabla^{\mu}\xi - e^{-4\chi}f_{\mu\nu}\tilde{f}^{\mu\nu} = 0 \\ \nabla_{\mu}\tilde{f}^{\mu\nu} = 0 \\ \nabla_{\mu}(e^{-2\chi}f^{\mu\nu} + \xi\tilde{f}^{\mu\nu}) = 0 \\ G_{\mu\nu} = e^{2\chi}(4f_{\mu\rho}f_{\nu}^{\rho} - g_{\mu\nu}f^2) - g_{\mu\nu}(2\nabla_{\mu}\chi\nabla^{\mu}\chi + \frac{1}{2}e^{4\chi}\nabla_{\mu}\xi\nabla^{\mu}\xi) \\ + \nabla_{\mu}\chi\nabla_{\nu}\chi + e^{4\chi}\nabla_{\mu}\xi\nabla_{\nu}\xi. \end{array} \right. \quad (2)$$

It demonstrates that the dilaton field, axion field, electromagnetic field, and gravitational field are intricately coupled. The axisymmetric classical solution known as the Kerr-Sen black hole can be derived in the Boyer-Lindquist coordinates, and it takes the following form [63].

$$ds^2 = - \left(1 - \frac{2Mr}{\tilde{\Sigma}}\right) dt^2 + \frac{\tilde{\Sigma}}{\tilde{\Delta}} dr^2 + \tilde{\Sigma} d\theta^2 - \frac{4aMr}{\tilde{\Sigma}} \sin^2\theta dt d\phi \\ + \sin^2\theta d\phi^2 \left(r(r+r_2) + a^2 + \frac{2Mra^2 \sin^2\theta}{\tilde{\Sigma}} \right), \quad (3)$$

with

$$\left\{ \begin{array}{l} \tilde{\Sigma} = r(r+r_2) + a^2 \cos^2\theta \\ \tilde{\Delta} = r(r+r_2) - 2Mr + a^2, \end{array} \right. \quad (4)$$

where M represents the mass parameter of the black hole, the dilation parameter $r_2 = \frac{Q^2}{M}$ is determined by the electric charge Q and a denotes the black hole's angular momentum per unit mass. Equation (3) indicates that upon removing the black hole's rotation parameter, a spherically symmetric dilaton black hole remains, characterized by mass, electric charge, and asymptotic value [63]. When the dilaton parameter r_2 becomes zero, the Kerr-Sen solution reverts to the Kerr black hole.

The black hole's event horizon r_{\pm} is specified by $\tilde{\Delta} = 0$, so we can get

$$\left\{ \begin{array}{l} r_+ = M - \frac{r_2}{2} + \sqrt{\left(M - \frac{r_2}{2}\right)^2 - a^2} \\ r_- = M - \frac{r_2}{2} - \sqrt{\left(M - \frac{r_2}{2}\right)^2 - a^2}. \end{array} \right. \quad (5)$$

Equation (5) establishes the theoretical range for the existence of internal and external event horizons as $0 \leq \frac{r_2}{M} \leq 2(1 - \frac{a}{M})$ or $-(1 - \frac{r_2}{2M}) \leq \frac{a}{M} \leq 1 - \frac{r_2}{2M}$. As the spin parameter a

is constrained by not exceeding the black hole mass M , we deduce that the theoretical effective range for r_2 is $0 \leq \frac{r_2}{M} \leq 2$. Figure 1 depicts the black hole region within the allowed parameter range ($r_+ > r_-$), while the white region represents the naked singularity appear ($r_- > r_+$).

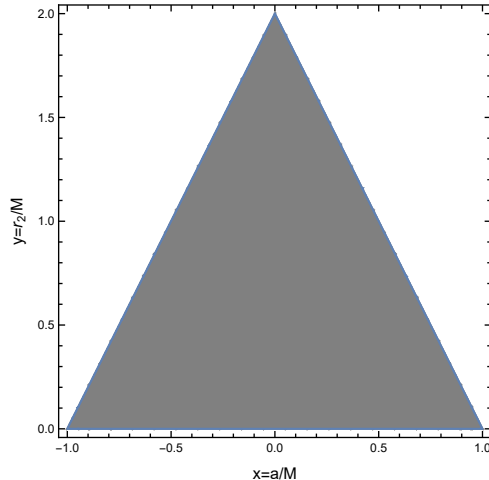


FIG. 1. On the horizontal axis, we have the dimensionless black hole parameter a , while the vertical axis represents the dimensionless dilaton parameter r_2 . The gray area corresponds to the black hole region, whereas the white area denotes the naked singularity.

III. THE PHYSICAL PROPERTIES OF THIN ACCRETION DISKS

In this section, we will calculate the radiant energy flux, radiation temperature, and observed luminosity from the accretion disc within the permissible interval $0 \leq \frac{r_2}{M} \leq 0.4$. This analysis enables the exploration of the observable effects of the Kerr-Sen black hole and offers an approach to distinguish it from the Kerr black hole. We adopt the fundamental feature of the Novikov-Thorne model to delineate the continuum spectrum [64]. The model incorporates several pivotal assumptions: (1) the primary contribution to the continuum spectrum originates from electromagnetic emission from the accretion disk surrounding the black hole; (2) the spacetime around the central massive object is both stationary and axisymmetric; (3) the mass of the accretion disk does not influence the background metric; (4) the accretion disk is geometrically thin, with vertical size considered negligible compared to its horizontal size; (5) the particles around the compact central object traverse between the outer edge (r_{out}) and the radius of the innermost stable circular orbit (r_{ISCO}) which defined as the inner edge of the disk; (6) the accretion disk is situated in the equatorial

plane of the accreting compact object, with the spin of the black hole perpendicular to the disk surface.

A. Timelike geodesics equations

The formation of an accretion disk is a result of particles moving along geodesic paths in orbits around a compact central object. However, the motion of particles are entirely dependent on the background geometry and the structure of the metric for a stationary axisymmetric spacetime is expressed as

$$ds^2 = g_{tt} dt^2 + 2g_{t\phi} dt d\phi + g_{rr} dr^2 + g_{\theta\theta} d\theta^2 + g_{\phi\phi} d\phi^2, \quad (6)$$

In Eq.(6), owing to the symmetry of the spacetime, the metric components g_{tt} , $g_{t\phi}$, g_{rr} , $g_{\theta\theta}$, and $g_{\phi\phi}$ solely rely on the variables r and θ . It is evident that within the aforementioned geometry, the motion exhibits two conserved quantities: the specific energy at infinity denoted as \tilde{E} , and the z -component of the specific angular momentum \tilde{L} at infinity. These quantities can be obtained by

$$\begin{cases} g_{tt} \frac{dt}{d\tau} + g_{t\phi} \frac{d\phi}{d\tau} = -\tilde{E} \\ g_{t\phi} \frac{dt}{d\tau} + g_{\phi\phi} \frac{d\phi}{d\tau} = \tilde{L}, \end{cases} \quad (7)$$

where τ denotes the affine parameter. In the equatorial plane characterized by $\theta = \frac{\pi}{2}$, the geodesic equation can be derived as follows

$$\begin{cases} \frac{dt}{d\tau} = \frac{\tilde{E}g_{\phi\phi} + \tilde{L}g_{t\phi}}{g_{t\phi}^2 - g_{tt}g_{\phi\phi}} \\ \frac{d\phi}{d\tau} = -\frac{\tilde{E}g_{t\phi} + \tilde{L}g_{tt}}{g_{t\phi}^2 - g_{tt}g_{\phi\phi}} \\ g_{rr} \left(\frac{dr}{d\tau} \right)^2 = V_{eff}(r), \end{cases} \quad (8)$$

with the effective potential

$$V_{eff} = \frac{\tilde{E}^2 g_{\phi\phi} + 2\tilde{E}\tilde{L}g_{t\phi} + \tilde{L}^2 g_{tt}}{g_{t\phi}^2 - g_{tt}g_{\phi\phi}} - 1. \quad (9)$$

The effective potential can be analogized to the Newtonian gravitational potential, as it provides the condition under which particles undergo circular orbital motion. The circular

orbit within the equatorial plane ($\theta = \frac{\pi}{2}$) is defined by the conditions $V_{eff}(r) = 0$ and $V_{eff,r}(r) = 0$. These conditions establish the specific energy \tilde{E} and the specific angular momentum \tilde{L} as functions of the angular velocity Ω of particles.

$$\begin{cases} \tilde{E} = \frac{-g_{tt} - \Omega g_{t\phi}}{\sqrt{-g_{tt} - 2\Omega g_{t\phi} - \Omega^2 g_{\phi\phi}}} \\ \tilde{L} = \frac{g_{t\phi} + \Omega g_{\phi\phi}}{\sqrt{-g_{tt} - 2\Omega g_{t\phi} - \Omega^2 g_{\phi\phi}}}, \end{cases} \quad (10)$$

where the angular velocity of the test particle Ω is

$$\Omega = \frac{d\phi}{dt} = \frac{-g_{t\phi,r} \pm \sqrt{(-g_{t\phi,r})^2 - g_{\phi\phi,r} g_{tt,r}}}{g_{\phi\phi,r}}. \quad (11)$$

Furthermore, to ascertain the inner edge of the disk, it is imperative to identify the innermost stable circular orbit (ISCO) of the black hole potential [65]. This involves utilizing the condition $V_{eff,rr}(r) = 0$, which leads to the derivation of the following relation.

$$\tilde{E}^2 g_{\phi\phi,rr} + 2\tilde{E}\tilde{L}g_{t\phi,rr} + \tilde{L}^2 g_{tt,rr} - (g_{t\phi}^2 - g_{tt}g_{\phi\phi})_{,rr} = 0. \quad (12)$$

For $r < r_{ISCO}$, the equatorial circular orbits are stable, so r_{ISCO} determines the inner edge of the thin accretion disk [20]. In Fig.2, we illustrate the variations of particle angular velocity, specific energy, specific angular momentum and r_{ISCO} with respect to the distance r and the black hole spin parameter a .

Based on Fig.2, we see that the angular velocity of the Kerr black hole surpasses that of the Kerr-Sen black hole under the condition of a fixed distance r . As the distance r increases, the angular velocity exhibits a decreasing trend. However, the specific energy \tilde{E} and specific angular momentum \tilde{L} demonstrate distinct patterns. It is worth noting that both \tilde{E} and \tilde{L} exhibit higher magnitudes in GR compared to the EMDA theory. Furthermore, as the parameter r_2 increases, the trend transitions from a decrease to increase, while the deviation from the Kerr black hole notably diminishes, eventually converging. Additionally, from the last diagram, we obtain that within the allowed parameter range, as the parameter a increases, the innermost stable circular orbit gradually decreases for different r_2 .

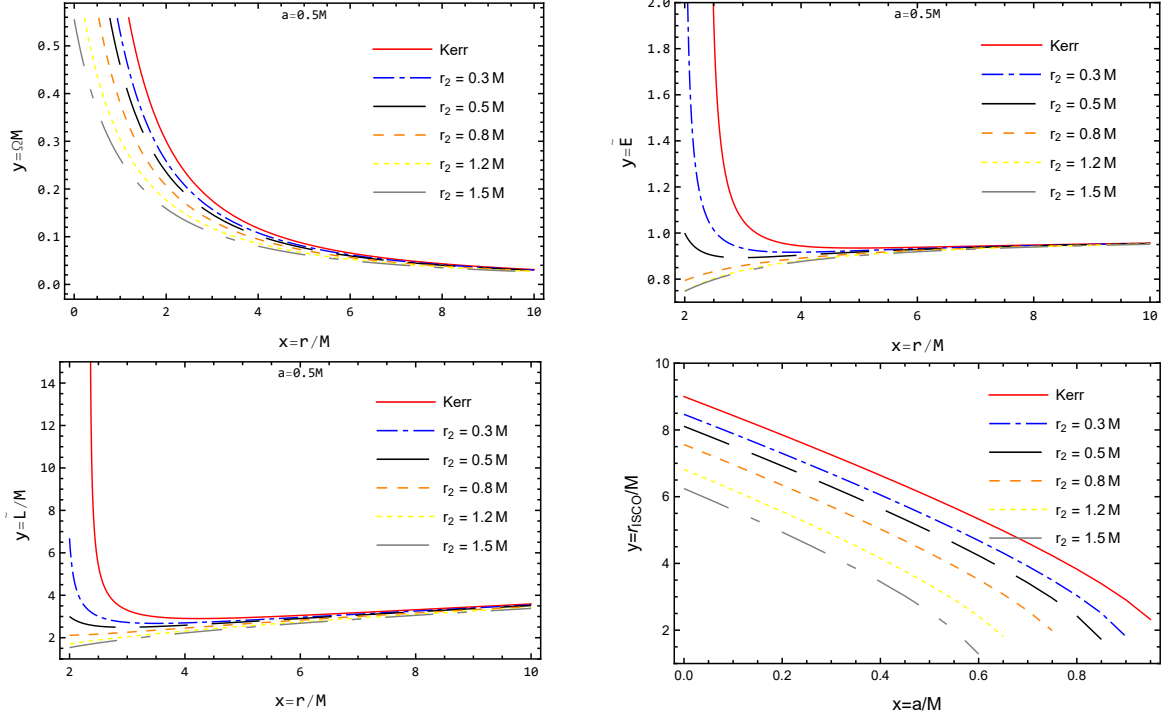


FIG. 2. The angular velocity Ω (top-left panel), the specific energy \tilde{E} (top-right panel), and the specific angular momentum \tilde{L} (bottom-left panel) are shown as a function of the radial coordinate r for different values of r_2 with $\frac{a}{M} = 0.5$. In bottom-right panel, r_{ISCO} illustrates the variation of a under different dilaton parameters r_2 .

B. Continuum Spectrum in the Kerr-Sen black hole

In model of steady-state accretion disks, the matter undergoing accretion in the disk can be characterized by an anisotropic fluid with the energy-momentum tensor [10, 11]

$$T_{\mu\nu} = \epsilon_0 u_\mu u_\nu + 2u_{(\mu} q_{\nu)} + t_{\mu\nu}, \quad (13)$$

where the terms ϵ_0 , q_μ , and $t_{\mu\nu}$ represent the rest mass density, energy flow vector, and stress tensor, respectively. These quantities are defined in the averaged rest-frame of the orbiting particle with the four-velocity u_μ . In the rest-frame, $t_{\mu\nu}$ and q_μ are orthogonal to u_μ ($u^\mu q_\mu = 0$ and $u^\mu t_{\mu\nu} = 0$). Furthermore, the motion of particles along geodesics ensures that the gravitational pull of the central black hole dominates the forces due to radial pressure gradients, and the specific internal energy of the accreting fluid can be ignored compared to its rest energy.

To calculate the flux and the luminosity emanating from the accretion disc, we assume that the accreting fluid adheres to the conservation of mass, energy, and angular momentum, which take the form

$$\begin{cases} \dot{M} = -2\pi\sqrt{-\tilde{g}}\Sigma(r)u^r = \text{const} \\ \left(\dot{M}\tilde{E} - 2\pi\sqrt{-\tilde{g}}\Omega W_\phi^r\right)_{,r} = 2\pi\sqrt{-\tilde{g}}F(r)\tilde{E} \\ \left(\dot{M}\tilde{L} - 2\pi\sqrt{-\tilde{g}}W_\phi^r\right)_{,r} = 2\pi\sqrt{-\tilde{g}}F(r)\tilde{L}, \end{cases} \quad (14)$$

with

$$\begin{cases} \Sigma(r) = \int_{-H}^H \langle \epsilon_0 \rangle dz \\ W_\phi^r = \int_{-H}^H \langle t_\phi^r \rangle dz \\ \sqrt{-\tilde{g}} = \sqrt{-\det \tilde{g}_{\mu\nu}}, \end{cases} \quad (15)$$

where $\Sigma(r)$ and W_ϕ^r are the averaged rest mass density and the averaged stress tensor, respectively. \tilde{g} corresponds to the determinant of the near-equatorial metric in cylindrical coordinates and the quantity $\langle t_\phi^r \rangle$ denotes the average value of the stress tensor during a certain period. Utilizing the energy-angular momentum relation for circular geodesic orbits $\tilde{E}_{,r} = \Omega\tilde{L}_{,r}$, one can eliminate W_ϕ^r from Eq.(14). Subsequently, this enables the derivation of the expression for the energy flux.

$$F(r) = -\frac{\dot{M}}{4\pi\sqrt{-\tilde{g}}} \frac{\Omega_{,r}}{(\tilde{E} - \Omega\tilde{L})^2} \int_{r_{ISCO}}^r (\tilde{E} - \Omega\tilde{L})\tilde{L}_{,r} dr. \quad (16)$$

Specifically, the above expression is only applicable for cylindrical coordinates. If we want to use it for spherical coordinates, it takes the form [66]

$$F(r) = -\frac{c^2\dot{M}}{4\pi\sqrt{-g/g_{\theta\theta}}} \frac{\Omega_{,r}}{(\tilde{E} - \Omega\tilde{L})^2} \int_{r_{ISCO}}^r (\tilde{E} - \Omega\tilde{L})\tilde{L}_{,r} dr, \quad (17)$$

where we have recovered the dimensions, and c denotes the speed of light. In this scenario, we examine mass accretion propelled by black holes with a total mass of $M = 2 \times 10^6 M_\odot$ and a corresponding mass accretion rate $\dot{M} = 2 \times 10^{-6} M_\odot yr^{-1}$. Figure 3 shows the energy flux $F(r)$ of the disk around Kerr-Sen black hole for different dilaton values r_2 . We observe that the distribution of the entire energy flux exhibits a trend of initially increasing, reaching a peak, and finally decreasing. The horizontal axis represents the dimensionless coordinate distance r , while the vertical axis denotes the order of magnitude of the energy flux. We

also conclude that as the black hole parameter r_2 increases within the allowed range, the black hole energy flux also increases, surpassing that of the Kerr black hole.

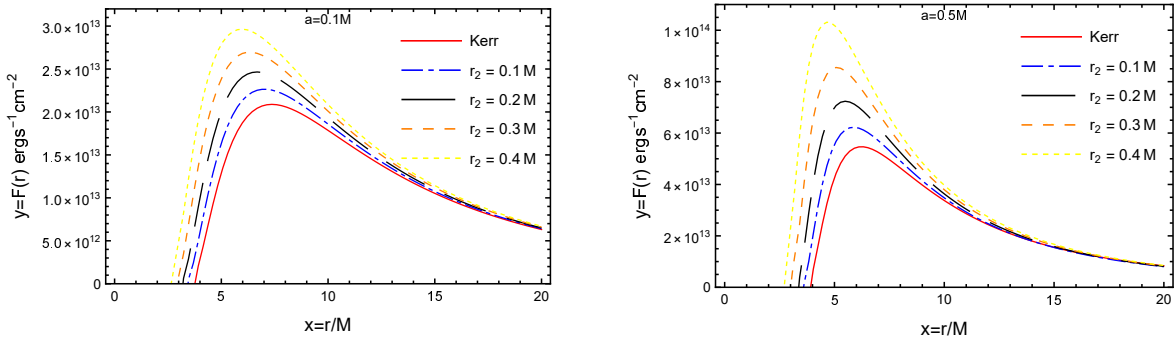


FIG. 3. The energy flux $F(r)$ of an accretion disk around the Kerr-Sen black hole for different values of the dilaton parameter r_2 with the spin parameter $\frac{a}{M} = 0.1$ (left) and $\frac{a}{M} = 0.5$ (right). we set the mass of sun $M_{\odot} = 1.989 \times 10^{33}$ g. The dashed line represents the radiation scenario for the Kerr black hole.

Within the framework of the Novikov-Thorne model, the accreted matter is assumed to be in thermodynamic equilibrium. This implies that the radiation emitted by the disk can be treated as perfect black body radiation. The radiation temperature $T(r)$ of the disk is related to the energy flux $F(r)$ through the Stefan-Boltzmann law, expressed as $F(r) = \sigma_{SB}T^4$, where σ_{SB} denotes the Stefan-Boltzmann constant. This suggests that the variation of $T(r)$ with respect to r is similar to the dependence of the energy flux $F(r)$ on r . In Fig.4, we plot the radiation temperature $T(r)$ around the Kerr-Sen black hole for the dilaton parameter r_2 and the rotation parameter a . Similar to the result for the energy flux, we find that as the parameter r_2 increases, the radiation temperature also increases, reaching its maximum value. Subsequently, the temperature decreases as the the distance r increasing.

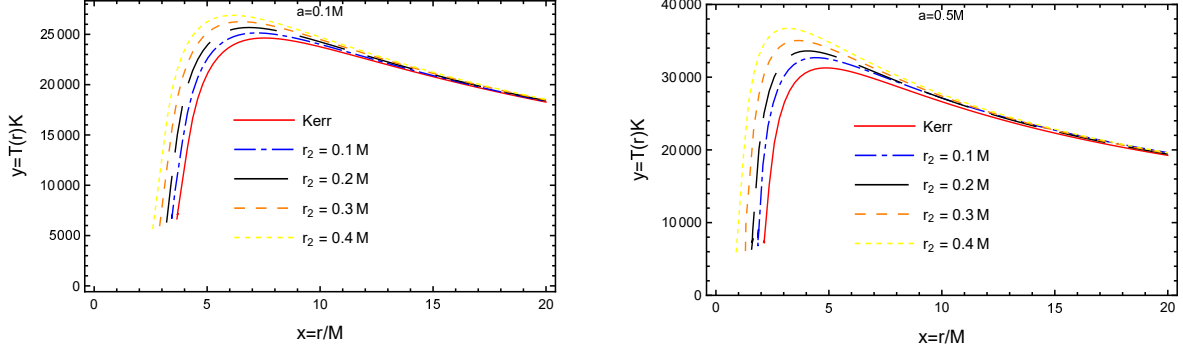


FIG. 4. The temperature $T(r)$ with the dilaton parameter r_2 in the thin disk. Here, we use the Stefan-Boltzmann constant $\sigma_{SB} = 5.67 \times 10^{-5} \text{ ergs}^{-1} \text{ cm}^{-2} \text{ K}^{-4}$ with fix rotation parameter $\frac{a}{M} = 0.1$ and $\frac{a}{M} = 0.5$, respectively.

The observed luminosity and the efficiency of matter accretion stand as crucial measurement parameters in the accretion process. The luminosity $L(\nu)$ is associated with the alteration in frequency of a photon as it travels from the emitting source to the observer [59, 67]. The maximum efficiency ϵ is determined by the specific binding energy at the marginally stable orbit r_{ISCO} [10, 64, 68]. These two physical quantities are

$$\begin{cases} L(\nu) = 4\pi d^2 I(\nu) = \frac{8\pi h \cos \gamma}{c^2} \int_{r_i}^{r_f} \int_0^{2\pi} \frac{\nu_e^3 r \, dr \, d\phi}{e^{h\nu_e/kT(r)} - 1} \\ \epsilon = 1 - E_{ISCO}(r_{ISCO}), \end{cases} \quad (18)$$

The emitted frequency is denoted by $\nu_e = \nu(1+z)$, and the redshift factor g can be defined as

$$g \equiv 1 + z = \frac{1 + \Omega r \sin \phi \sin \gamma}{\sqrt{-g_{tt} - 2\Omega g_{t\phi} - \Omega^2 g_{\phi\phi}}}. \quad (19)$$

where E_{ISCO} is the specific energy of the test particle at r_{ISCO} , h is Planck constant, and k is the Boltzmann constant. The γ and d represent the inclination angle of the accretion disk and the distance from the observer to the disk center. $L(\nu)$ is the thermal energy flux radiated by the disk. To determine the luminosity $L(\nu)$ of the disk, we consider $r_i = r_{ISCO}$ and $r_f = \infty$ since the flux over the disk surface decreases as $r \rightarrow \infty$ in the rotating Kerr-Sen black hole.

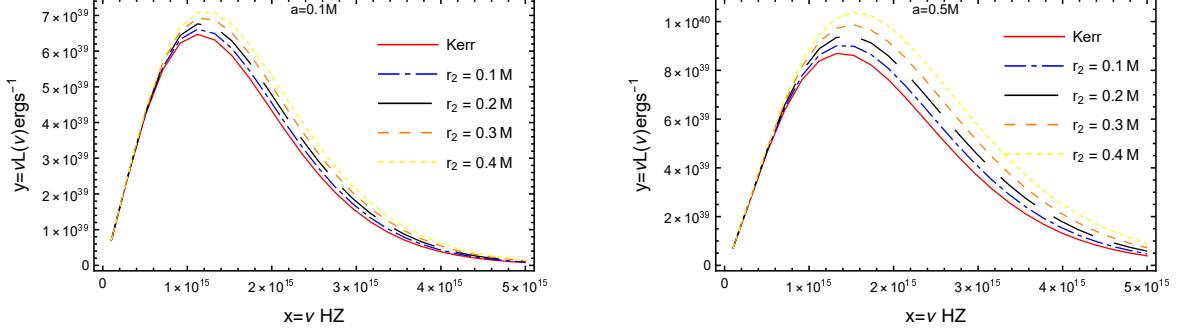


FIG. 5. The emission spectrum $\nu L(\nu)$ of accretion disk around Kerr-Sen black hole for different r_2 with spin parameter $\frac{a}{M} = 0.1$ (left) and $\frac{a}{M} = 0.5$ (right). The inclination angle is $\gamma = 0^\circ$.

The variations of spectral energy distribution are illustrated in Fig.5. The two figures illustrate the variations in $\nu L(\nu)$ with the dilaton parameter r_2 with $\frac{a}{M} = 0.1$ and $\frac{a}{M} = 0.5$. Initially, the entire spectrum exhibits a blackbody distribution with the peak occurring at high frequencies. However, we can't distinguish different black holes at lower frequencies. Additionally, as the black hole parameter r_2 increases, a noticeable rightward shift in the peak is observed, which indicates greater emitted energy compared to the Kerr black hole. This conclusion is consistent with the Ref.[59], though the luminosity formula and the consideration of model parameters differ.

In our previous work, we have provided conclusion on the radiation efficiency [56]. It shows that the radiative efficiency of the Kerr-Sen black hole increases with the growth of the parameter r_2 (or the parameter a). In addition, the efficiency of the Kerr-Sen black hole surpasses that of the Kerr black hole with fixed parameter. This observation contributes to a deeper understanding of these two black holes through empirical observations.

IV. BLACK HOLE SHADOW IN PLASMA ENVIRONMENT

In this section, we will explore the shadow of the Kerr-Sen black hole within a homogeneous plasma environment. The study of radiation propagation through an isotropic and dispersive medium in GR was initially conducted by Bicak and Hadrava in 1975 [69]. Additionally, the shadow of various black holes in the presence of plasma has been explored in Refs.[60, 70–85]. Here, we examine the effect of the plasma parameter on the black hole shadow image in the Kerr-Sen black hole. Furthermore, we will use observational data from the EHT to constrain the model parameters.

A. Hamilton-Jacobi equation for null geodesics in plasma

We consider a straightforward scenario involving a cold (pressureless) and nonmagnetized plasma, where the behavior of light is governed by the Hamiltonian [73, 74, 84–86]

$$H(x, p) = \frac{1}{2} (g^{\mu\nu} p_\mu p_\nu + \omega_p^2(x)), \quad (20)$$

where ω_p represents the plasma electron frequency given by

$$\omega_p^2(x) \equiv \frac{4\pi e^2}{m_e} N(x), \quad (21)$$

m_e and e represent the mass and charge of the electron, respectively, while $N(x)$ describes the distribution of electron density. Here, x denotes the spacetime coordinates (t, r, θ, ϕ) and p refers to the momentum coordinates $(p_t, p_r, p_\theta, p_\phi)$. Additionally, the plasma frequency ω_p and the photon frequency ω are related by refractive index n , which can be defined as

$$n^2 \equiv 1 - \frac{\omega_p^2(x)}{\omega^2(x)}. \quad (22)$$

Taking into account the gravitational redshift effect on the constant of motion $p_t \equiv -\omega_0$, the frequency of the observed redshift is given by $\omega(x) = \frac{\omega_0}{\sqrt{-g_{00}}}$. Since the refractive index $n > 0$, the condition for generalized rotating metric can be given by [84, 85]

$$\omega_0^2 > -g_{tt}\omega_p^2(x). \quad (23)$$

We will explore the homogeneous plasma distribution described by the equation $\omega_p^2 = k\omega_0^2$ spanning the region between the observer and the horizon. Here, k represents the homogeneous plasma parameter, which must fall within the interval $(0 < k < 1)$ to adhere to Eq. (23). Subsequently, let's consider the Hamilton-Jacobi equation for the null geodesics as

$$H\left(x, \frac{\partial S}{\partial x^\mu}\right) = \frac{1}{2} g^{\mu\nu} \frac{\partial S}{\partial x^\mu} \frac{\partial S}{\partial x^\nu} + \frac{1}{2} \omega_p^2(x) = 0, \quad (24)$$

with the separation ansatz

$$S = -\omega_0 t + L_z \phi + S_r(r) + S_\theta(\theta), \quad (25)$$

where L_z represents conserved quantity of photons along the ϕ direction. Given that our study focuses on the variation of coordinates r and θ within a plasma environment, separation of the above equation is feasible only if we adopt a general expression for the plasma

frequency in the Kerr-Sen black hole, as follows [87, 88]

$$\omega_p^2 = \frac{f_r(r) + f_\theta(\theta)}{\tilde{\Sigma}}. \quad (26)$$

In the uniform plasma system, $f_r(r)$ and $f_\theta(\theta)$ can each be assigned the values $k\omega_0^2 r(r+r_2)$ and $k\omega_0^2 a^2 \cos^2 \theta$. Now, using Eq.(24), Eq.(25) and Eq.(26), we get the following expressions

$$\begin{cases} \tilde{\Delta}^2 \left(\frac{dS}{dr} \right)^2 = -K\tilde{\Delta} - a^2\omega_0^2\tilde{\Delta} - \tilde{\Delta}L_z^2 - k\omega_0^2\tilde{\Delta}(r(r+r_2)) + a^2L_z^2 + \omega_0^2(r(r+r_2) + a^2)^2 \\ \left(\frac{dS}{d\theta} \right)^2 = K - k\omega_0^2 a^2 \cos^2 \theta - L_z^2 \cot^2 \theta + a^2\omega_0^2 \cos^2 \theta. \end{cases} \quad (27)$$

Where K is Carter's constant and $\frac{dS}{dx^\mu} = p_\mu$. By employing the Hamiltonian equations, we can simplify the equations of motion to

$$\begin{cases} \frac{dt}{d\lambda} = \frac{\omega_0}{\tilde{\Delta}\tilde{\Sigma}} \left((r(r+r_2) + a^2)^2 - \tilde{\Delta}a^2 \sin^2 \theta - 2Mra\xi \right) \\ \frac{d\phi}{d\lambda} = \frac{\omega_0}{\tilde{\Delta}\tilde{\Sigma}} \left(2Mra + \frac{\tilde{\Sigma} - 2Mr}{\sin^2 \theta} \xi \right) \\ \frac{dr}{d\lambda} = \pm \frac{1}{\tilde{\Sigma}} \sqrt{R(r)} \\ \frac{d\theta}{d\lambda} = \pm \frac{1}{\tilde{\Sigma}} \sqrt{\Theta(\theta)}, \end{cases} \quad (28)$$

with

$$\begin{cases} R(r) \equiv \omega_0^2 \left(a^2\xi^2 + (r(r+r_2) + a^2)^2 - 4Mra\xi - \tilde{\Delta}(\eta + a^2 + \xi^2 + kr(r+r_2)) \right) \\ \Theta(\theta) \equiv \omega_0^2 (\eta + a^2 \cos^2 \theta - \xi^2 \cot^2 \theta - ka^2 \cos^2 \theta). \end{cases} \quad (29)$$

Where λ is affine parameter and two impact parameters $\xi \equiv \frac{L_z}{\omega_0}$, $\eta = \frac{K}{\omega_0}$ characterize the system [60]. The parameter ξ denotes the distance from the axis of rotation, while η signifies the distance from the equatorial plane. It is worth noting that when the $k = 0$, the equation reduces to the photon trajectories of the vacuum case.

Since the shadow is created by the last photon rings, which are inherently unstable, null rays must meet the following conditions to maintain unstable spherical orbits [87],

$$\frac{d^2 R(r)}{dr^2} > 0, \Theta(\theta) \geq 0. \quad (30)$$

The first condition is necessary for these orbits to be unstable, while the second condition ensures the existence of spherical orbits around the Kerr-Sen black hole. A similar analysis for axially symmetric stationary spacetime can be found in Ref.[89].

B. The shadow of Kerr-Sen black hole in plasma spacetime

In the subsection, we focus on investigating the shadow distribution of Kerr-Sen black holes in a uniform plasma environment. Then, we will explore the effects of the dilaton parameter r_2 and the homogeneous plasma parameters k on the black hole shadow. To streamline our analysis, we will initially derive the general expression for the impact parameters corresponding to the boundary of shadow. Because the boundary offer crucial insights into the optical properties of the Kerr-Sen black hole, enriching our comprehension of its features and dynamics.

In order to determine the boundary of the Kerr-Sen black hole shadow, we analyze the radial motion described by Eq.(28). The boundary is defined by the circular photon orbit, which must satisfy the following conditions [90, 91]

$$R(r_c) = 0, \frac{dR(r_c)}{dr} = 0, \quad (31)$$

where r_c denotes the critical photon orbit. By solving these conditions, we obtain these expressions for the impact parameters as follows

$$\begin{cases} \xi = \frac{A_1 + 2M(a - r_c)(a + r_c)}{a(2M - 2r_c - r_2)} \\ \eta = \frac{r_c^2(4M(A_1 + A_2 + \frac{1}{2}A_3) + (2r_c + r_2)A_4)}{a^2(2M - 2r_c - r_2)^2}, \end{cases} \quad (32)$$

where

$$\begin{cases} A_1 \equiv (a^2 + r_c(r_c - 2M + r_2)) \sqrt{(2r_c + r_2)(k(2M - 2r_c - r_2) + 2r_c + r_2)} \\ A_2 \equiv M((8k - 5)r^2 + 2(5k - 2)r_2r + (3k - 1)r_2^2) \\ A_3 \equiv a^2(2k(M - r_c) - (k - 2)r_2 + 4r_c) \\ A_4 \equiv -8kM^3 - 2M(r + r_2)((5k - 4)r + (3k - 2)r_2) + (k - 1)(r + r_2)^2(2r + r_2). \end{cases} \quad (33)$$

As previously discussed, these critical orbits are essential in defining the last photon rings. Consequently, ξ and η can entirely delineate the shadow's boundary. Nonetheless, to visualize the shadow in the observer's sky, we utilize the following celestial coordinates [92]

$$\begin{cases} \alpha = \lim_{r_0 \rightarrow \infty} \left(r_0^2 \sin \theta \frac{d\phi}{dr} \Big|_{\theta \rightarrow \theta_0} \right) \\ \beta = \lim_{r_0 \rightarrow \infty} \left(r_0^2 \frac{d\theta}{dr} \Big|_{\theta \rightarrow \theta_0} \right), \end{cases} \quad (34)$$

where, r_0 represents the distance from the distant observer to the black hole, and θ_0 represents the inclination angle between the observer's line of sight and the black hole's spin axis. The parameters α and β give the shadow's profile. By the geodesic equation (28) and applying the condition for unstable circular orbit, we can simplify the celestial coordinates as follows

$$\begin{cases} \alpha = -\frac{\xi}{\sin \theta_0 \sqrt{1-k}} \\ \beta = \pm \frac{\sqrt{\eta - \xi^2 \cot^2 \theta_0 + (1-k)a^2 \cos^2 \theta_0}}{\sqrt{1-k}}. \end{cases} \quad (35)$$

It is crucial to recognize that these expressions do not apply in a vacuum distribution ($k = 0$). In particular, for a uniform distribution, the plasma density is pivotal in determining the shape of a black hole shadow. The panel (left) of Fig.6 illustrates the variation of the black hole shadow distribution in a uniform plasma environment with respect to the parameter k , while the panel (right) depicts the variation of the black hole shadow distribution with the parameter r_2 . We observe that as the parameter k increases, the black hole shadow gradually enlarges, while with the increase of the parameter r_2 , the black hole shadow decreases. These effects are also likely to be easily observed by low-resolution radio telescopes.

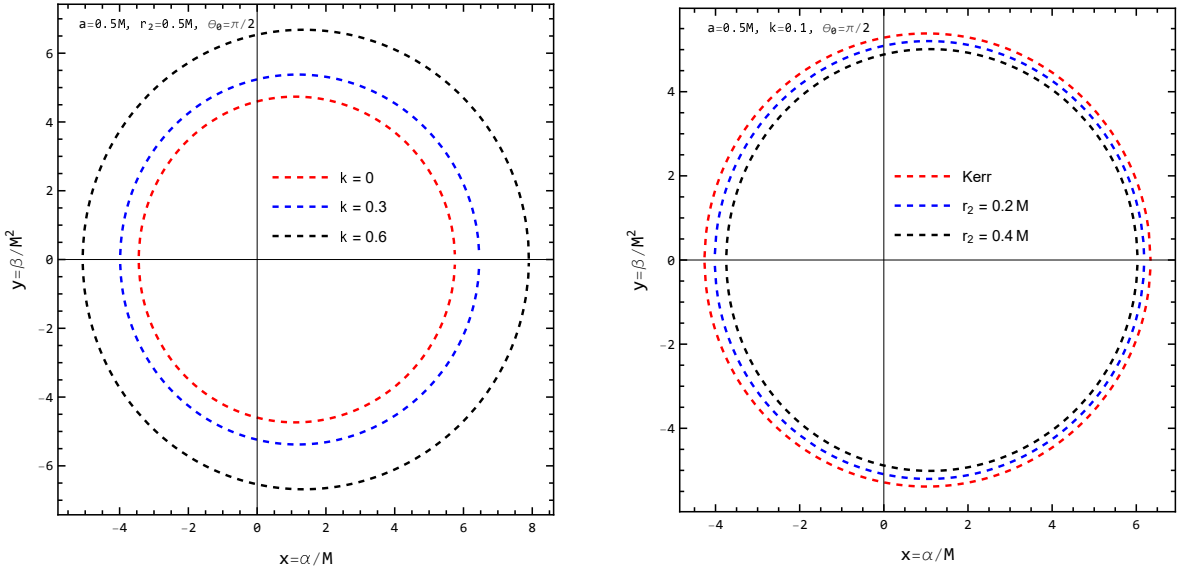


FIG. 6. The left figure depicts the image of the Kerr-Sen black hole shadow with fixed parameters $\frac{r_2}{M} = 0.5$, the inclination angle $\theta_0 = 90^\circ$, and the spin parameter $\frac{a}{M} = 0.5$ for different k . The right figure presents the shadow of the Kerr-Sen black hole, depicted with fixed parameters θ_0 , k and a for different r_2 .

C. Constraints on parameters with the EHT observations of M87* and Sgr A*

The EHT observations of M87* and Sgr A* provide constraints on theoretical models of black holes. By capturing the shadow and surrounding emission of these supermassive black holes, the EHT data allows researchers to refine parameters. These observations validate aspects of GR and alternative theories of gravity, offering unprecedented insights into the nature of black holes and their immediate environments. To constrain the parameter k and r_2 from shadow images, we utilize observational data from the EHT concerning the supermassive black hole at the M87* and Sgr A*.

According to Ref. [2, 3, 93], the angular diameter of the shadow of M87* is $\Delta\theta_{M87^*} = 42 \pm 3 \mu\text{as}$, the distance from Earth to the black hole is $D = 16.8 \text{ Mpc}$, and the mass of M87* is $M = (6.5 \pm 0.9) \times 10^9 M_\odot$. Conversely, the data for Sgr A* is sourced from the recent literature [4, 94], which reports the angular diameter of Sgr A* is $\Delta\theta_{SgrA^*} = 48.7 \pm 7 \mu\text{as}$, the distance is $D = 8277 \pm 33 \text{ pc}$, and the mass is $M = (4.3 \pm 0.013) \times 10^6 M_\odot$. Given these data, Ref. [78, 84, 85] estimates the diameter of the black hole shadow d_{sh} , which can be expressed as

$$\begin{cases} d_{sh}^{M87^*} = 2 \times D \times \tan \frac{\Delta\theta_{M87^*}}{2} \approx (11 \pm 1.5)M \\ d_{sh}^{SgrA^*} = 2 \times D \times \tan \frac{\Delta\theta_{SgrA^*}}{2} \approx (9.5 \pm 1.4)M. \end{cases} \quad (36)$$

Subsequently, to match the theoretical shadow diameter with observational data, we need to consider the shadow radius R_{sh} of the Kerr-Sen black hole. In this analysis, we will calculate only the case with an inclination angle of $\theta_0 = 90^\circ$. According to Ref. [81, 82, 95], the Kerr-Sen black hole shadow radius can be defined as

$$\begin{cases} R_{sh} = \frac{1}{2} (\alpha(r_{sp}^+) - \alpha(r_{sp}^-)) \\ \beta(r_{sp}^\pm) = 0, \end{cases} \quad (37)$$

where r_{sp}^\pm ($r_{sp}^+ > r_{sp}^-$) denotes the unstable photon orbits. It is noteworthy that photons at $\alpha(r_{sp}^+)$ and $\alpha(r_{sp}^-)$ typically originate from orbits rotating in the same and opposite directions as the black hole, respectively. Hence, the theoretical shadow diameter can be obtained via $d_{sh}^{theo} = 2R_{sh}$. Furthermore, by comparing the theoretical value with the observational data, we can constrain the range of the model parameters.

Figure 7 illustrates the variation in the shadow diameter as a function of the parameters k and r_2 for M87* and Sgr A*. The region outlined by black dashed lines represents the 1σ

confidence interval, while the area enclosed by blue dashed lines indicates the 2σ confidence interval. The top two panels illustrate the variation in the shadow diameter of the Kerr-Sen black hole with the dilaton parameter r_2 in a vacuum environment ($k = 0$) for a fixed parameter a . The bottom two panels depict the change in the shadow diameter of the Kerr-Sen black hole with the homogeneous plasma parameter k . The intersections of the dashed and solid lines indicate the upper limit of the parameter, which are provided in Tab.2 and Tab.3, respectively. It can be observed that in the vacuum case, the upper bound of the dilaton parameter r_2 decreases as the spin parameter a increases. Furthermore, for M87* data with $\frac{r_2}{M} = 0.1$, the homogeneous plasma parameter k decreases with increasing a within the 1σ interval and is allowed within the 2σ interval. For Sgr A* data, the parameter k is permitted within both the 1σ and 2σ intervals.

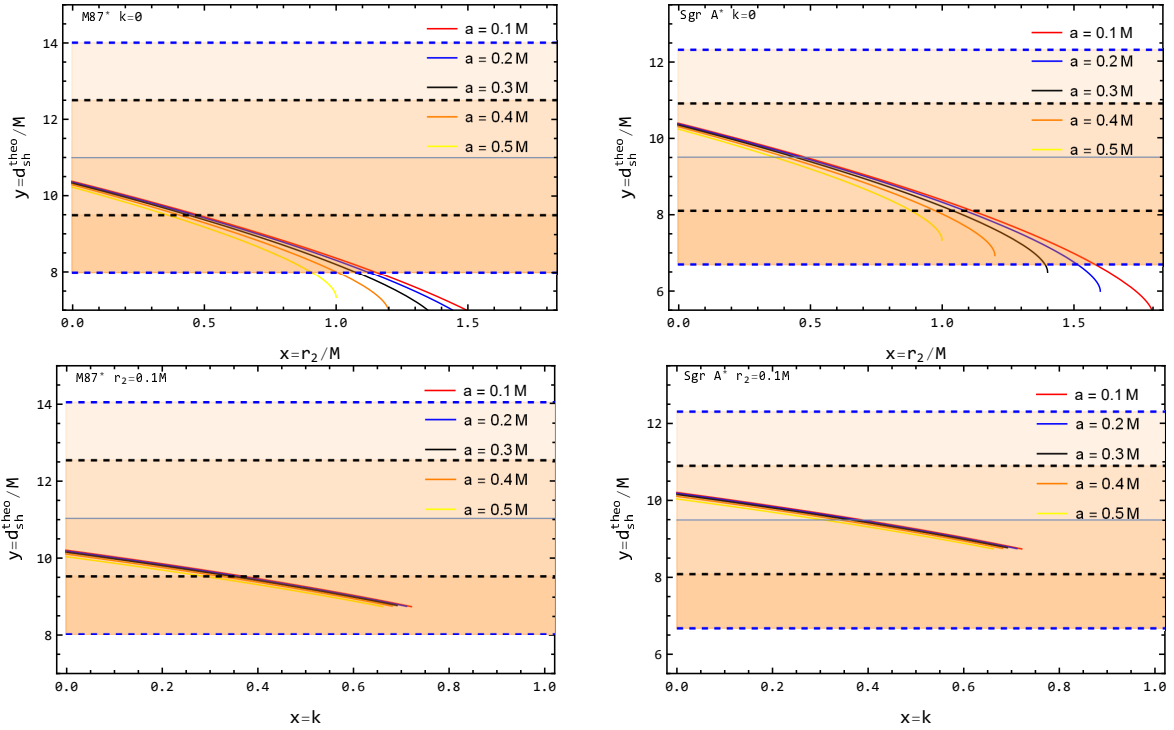


FIG. 7. The top two plots illustrate the constraints on the dilaton parameter r_2 within 1σ (The region bounded by two black dashed lines) and 2σ (The region bounded by two blue dashed lines) confidence intervals for different values of the spin parameter a in a vacuum environment ($k = 0$), using data from M87* (top-left) and Sgr A* (top-right). The bottom two plots depict the constraint on the homogeneous plasma parameter k with fixed parameter $\frac{r_2}{M} = 0.1$.

TABLE I. The ranges for the parameters constrained from M87* data. The dash indicates the absence of a corresponding parameter value.

M87*				M87*			
		1σ	2σ			1σ	2σ
$\frac{a}{M}$	k	Upper bound ($\frac{r_2}{M}$)	Upper bound ($\frac{r_2}{M}$)	$\frac{a}{M}$	$\frac{r_2}{M}$	Upper bound (k)	Upper bound (k)
0.1	0	0.480718	1.153510	0.1	0.1	0.38779	-
0.2	0	0.466644	1.125200	0.2	0.1	0.37887	-
0.3	0	0.442937	1.076700	0.3	0.1	0.36337	-
0.4	0	0.409200	1.005730	0.4	0.1	0.34019	-
0.5	0	0.364832	0.908329	0.5	0.1	0.30739	-

TABLE II. The ranges for the parameters constrained from Sgr A* data.

Sgr A*				Sgr A*			
		1σ	2σ			1σ	2σ
$\frac{a}{M}$	k	Upper bound ($\frac{r_2}{M}$)	Upper bound ($\frac{r_2}{M}$)	$\frac{a}{M}$	$\frac{r_2}{M}$	Upper bound (k)	Upper bound (k)
0.1	0	1.114420	1.579320	0.1	0.1	-	-
0.2	0	1.087590	1.512470	0.2	0.1	-	-
0.3	0	1.041720	1.389720	0.3	0.1	-	-
0.4	0	0.974817	-	0.4	0.1	-	-
0.5	0	0.883507	-	0.5	0.1	-	-

V. CONCLUSION AND DISCUSSION

In our investigation of rotating Kerr-Sen black hole within the EMDA framework, we focused on exploring the characteristics of thin relativistic accretion disks using the Novikov-Thorne model. Initially, we derived key physical quantities, including the effective potential V_{eff} , specific angular momentum \tilde{L} , specific energy \tilde{E} , angular velocity Ω , and the ISCO radius for test particles in circular orbits around the black hole. Since the ISCO radius lacked an analytical solution, we employed numerical methods to calculate it for various spin a and dilaton parameters r_2 . Our analysis revealed that, for a given a value, the ISCO radius decreases as the dilaton parameter increases. However, the specific angular momentum \tilde{L} and specific energy \tilde{E} of detected particle undergo changes with the dilaton

parameter r_2 . When the parameter exceeds a critical value, the function transitions from a decreasing to an increasing trend. Subsequently, the particle's angular velocity Ω exhibits a continuous decrease as r_2 increases.

Additionally, to calculate the heat emitted by the accretion disk, we performed numerical calculations to acquire the energy flux $F(r)$, temperature $T(r)$, and luminosity distribution $L(\nu)$, subsequently creating diagrams for these quantities. The results highlight the impact of the dilaton parameter r_2 and the spin parameter a on the observable quantities within the framework of the EMDA model. As the dilaton parameter r_2 increases from 0 to 0.4 M, affecting the energy flux, radiation temperature, and observed luminosity of the thin accretion disk. The differences of spectrum distributions reveal significant distinctions for the Kerr-Sen black hole compared to the Kerr black hole and also contribute to exploring through observations.

Furthermore, we investigated the shadow of the Kerr-Sen black hole in a uniform plasma background. First, we calculated the geodesic equations for photons in this environment. Then, we introduced celestial coordinates and determined the boundary of the black hole shadow by calculating the impact parameters ξ and η . We found that, for an observer's angle of 90° with $\frac{r_2}{M} = \frac{a}{M} = 0.5$, the black hole shadow gradually increases as the homogeneous plasma parameter k increases. However, when $k = 0.1$ and $\frac{a}{M} = 0.5$ are fixed, we observed that the shadow decreases as the dilaton parameter r_2 increases. This behavior can be distinguished through observations. Finally, using observational data from M87* and Sgr A*, we constrained the model parameters within the 1σ and 2σ intervals based on the black hole shadow diameter d_{sh} , thereby enhancing our understanding of black hole properties.

ACKNOWLEDGMENTS

This work was supported by the National Key R&D Program of China (Grants No. 2022YFA1403700), NSFC (Grants No. 12141402, 12334002, 12333008), the SUSTech-NUS Joint Research Program, Center for Computational Science and Engineering at Southern University of Science and Technology, and Hebei Provincial Natural Science Foundation of

China (Grant No. A2021201034).

- [1] B. P. Abbott et al. Observation of Gravitational Waves from a Binary Black Hole Merger. *Phys. Rev. Lett.*, 116(6):061102, 2016.
- [2] Kazunori Akiyama et al. First M87 Event Horizon Telescope Results. I. The Shadow of the Supermassive Black Hole. *Astrophys. J. Lett.*, 875:L1, 2019.
- [3] Kazunori Akiyama et al. First M87 Event Horizon Telescope Results. IV. Imaging the Central Supermassive Black Hole. *Astrophys. J. Lett.*, 875(1):L4, 2019.
- [4] Kazunori Akiyama et al. First Sagittarius A* Event Horizon Telescope Results. I. The Shadow of the Supermassive Black Hole in the Center of the Milky Way. *Astrophys. J. Lett.*, 930(2):L12, 2022.
- [5] Sourabh Nampalliwar and Cosimo Bambi. Accreting Black Holes. 10 2018.
- [6] Andrew King and Derek Raine. *Accretion Power in Astrophysics*. 01 2002.
- [7] Feng Yuan and Ramesh Narayan. Hot Accretion Flows Around Black Holes. *Ann. Rev. Astron. Astrophys.*, 52:529–588, 2014.
- [8] N. I. Shakura and R. A. Sunyaev. Black holes in binary systems. Observational appearance. *Astron. Astrophys.*, 24:337–355, 1973.
- [9] I. D. Novikov and K. S. Thorne. Astrophysics of black holes. In *Black Holes (Les Astres Occlus)*, pages 343–450, January 1973.
- [10] Don N. Page and Kip S. Thorne. Disk-Accretion onto a Black Hole. Time-Averaged Structure of Accretion Disk. *Astrophys. J.*, 191:499–506, 1974.
- [11] Kip S. Thorne. Disk accretion onto a black hole. 2. Evolution of the hole. *Astrophys. J.*, 191:507–520, 1974.
- [12] V. Perlick. *Ray Optics, Fermat’s Principle, and Applications to General Relativity*. Lecture Notes in Physics Monographs. Springer, 2000.
- [13] João Luís Rosa, Daniela S. J. Cordeiro, Caio F. B. Macedo, and Francisco S. N. Lobo. Observational imprints of gravastars from accretion disks and hot-spots. 1 2024.
- [14] João Luís Rosa, Caio F. B. Macedo, and Diego Rubiera-Garcia. Imaging compact boson stars with hot spots and thin accretion disks. *Phys. Rev. D*, 108(4):044021, 2023.
- [15] Tong-Yu He, Ziqiang Cai, and Rong-Jia Yang. Thin accretion disks around a black hole in

- Einstein-Aether-scalar theory. *Eur. Phys. J. C*, 82(11):1067, 2022.
- [16] Malihe Heydari-Fard, Sara Ghassemi Honarvar, and Mohaddese Heydari-Fard. Thin accretion disc luminosity and its image around rotating black holes in perfect fluid dark matter. *Mon. Not. Roy. Astron. Soc.*, 521(1):708–716, 2023.
- [17] G. Abbas, Hamza Rehman, M. Usama, and Tao Zhu. Accretion disc around black hole in Einstein-SU(N) non-linear sigma model. *Eur. Phys. J. C*, 83(5):422, 2023.
- [18] Changqing Liu, Chikung Ding, and Jiliang Jing. Thin accretion disk around a rotating Kerr-like black hole in Einstein-bumblebee gravity model. 10 2019.
- [19] R. Kh. Karimov, R. N. Izmailov, Amrita Bhattacharya, and K. K. Nandi. Accretion disks around the Gibbons–Maeda–Garfinkle–Horowitz–Strominger charged black holes. *Eur. Phys. J. C*, 78(9):788, 2018.
- [20] Shahab Shahidi, Tiberiu Harko, and Zoltán Kovács. Distinguishing Brans–Dicke–Kerr type naked singularities and black holes with their thin disk electromagnetic radiation properties. *Eur. Phys. J. C*, 80(2):162, 2020.
- [21] Mohaddese Heydari-Fard, Malihe Heydari-Fard, and Hamid Reza Sepangi. Thin accretion disks and charged rotating dilaton black holes. *Eur. Phys. J. C*, 80(4):351, 2020.
- [22] Jonathan R. Gair, Chao Li, and Ilya Mandel. Observable Properties of Orbits in Exact Bumpy Spacetimes. *Phys. Rev. D*, 77:024035, 2008.
- [23] Cosimo Bambi and Enrico Barausse. Constraining the quadrupole moment of stellar-mass black-hole candidates with the continuum fitting method. *Astrophys. J.*, 731:121, 2011.
- [24] Sudip Bhattacharyya, Arun V. Thampan, and Ignazio Bombaci. Temperature profiles of accretion discs around rapidly rotating strange stars in general relativity: a comparison with neutron stars. *Astron. Astrophys.*, 372:925, 2001.
- [25] Z. Kovacs, K. S. Cheng, and T. Harko. Thin accretion disks around neutron and quark stars. *Astron. Astrophys.*, 500:621–631, 2009.
- [26] F. Siddhartha Guzman. Accretion disc onto boson stars: A Way to supplant black holes candidates. *Phys. Rev. D*, 73:021501, 2006.
- [27] J. L. Synge. The Escape of Photons from Gravitationally Intense Stars. *Mon. Not. Roy. Astron. Soc.*, 131(3):463–466, 1966.
- [28] J. P. Luminet. Image of a spherical black hole with thin accretion disk. *Astron. Astrophys.*, 75:228–235, 1979.

- [29] Alexander F. Zakharov. Constraints on a charge in the reissner-nordström metric for the black hole at the galactic center. *Phys. Rev. D*, 90:062007, Sep 2014.
- [30] Rohta Takahashi. Black hole shadows of charged spinning black holes. *Publ. Astron. Soc. Jap.*, 57:273, 2005.
- [31] Naoki Tsukamoto. Black hole shadow in an asymptotically flat, stationary, and axisymmetric spacetime: The kerr-newman and rotating regular black holes. *Phys. Rev. D*, 97:064021, Mar 2018.
- [32] Pedro V. P. Cunha, Carlos A. R. Herdeiro, Eugen Radu, and Helgi F. Rúnarsson. Shadows of kerr black holes with scalar hair. *Phys. Rev. Lett.*, 115:211102, Nov 2015.
- [33] Zilong Li and Cosimo Bambi. Measuring the Kerr spin parameter of regular black holes from their shadow. *JCAP*, 01:041, 2014.
- [34] Ahmadjon Abdujabbarov, Muhammed Amir, Bobomurat Ahmedov, and Sushant G. Ghosh. Shadow of rotating regular black holes. *Phys. Rev. D*, 93(10):104004, 2016.
- [35] Muhammed Amir and Sushant G. Ghosh. Shapes of rotating nonsingular black hole shadows. *Phys. Rev. D*, 94(2):024054, 2016.
- [36] Pedro V. P. Cunha, Carlos A. R. Herdeiro, Burkhard Kleihaus, Jutta Kunz, and Eugen Radu. Shadows of Einstein–dilaton–Gauss–Bonnet black holes. *Phys. Lett. B*, 768:373–379, 2017.
- [37] Farruh Atamurotov, Ahmadjon Abdujabbarov, and Bobomurat Ahmedov. Shadow of rotating non-kerr black hole. *Phys. Rev. D*, 88:064004, Sep 2013.
- [38] Mingzhi Wang, Songbai Chen, and Jiliang Jing. Shadow casted by a Konoplya-Zhidenko rotating non-Kerr black hole. *JCAP*, 10:051, 2017.
- [39] Akhil Uniyal, Sara Kanzi, and İzzet Sakallı. Some observable physical properties of the higher dimensional dS/AdS black holes in Einstein-bumblebee gravity theory. *Eur. Phys. J. C*, 83(7):668, 2023.
- [40] Ahmadjon Abdujabbarov, Farruh Atamurotov, Naresh Dadhich, Bobomurat Ahmedov, and Zdeněk Stuchlík. Energetics and optical properties of 6-dimensional rotating black hole in pure Gauss–Bonnet gravity. *Eur. Phys. J. C*, 75(8):399, 2015.
- [41] Mert Okyay and Ali Övgün. Nonlinear electrodynamics effects on the black hole shadow, deflection angle, quasinormal modes and greybody factors. *JCAP*, 01(01):009, 2022.
- [42] Misba Afrin, Sunny Vagnozzi, and Sushant G. Ghosh. Tests of Loop Quantum Gravity from the Event Horizon Telescope Results of Sgr A*. *Astrophys. J.*, 944(2):149, 2023.

- [43] Farruh Atamurotov and Bobomurat Ahmedov. Optical properties of black hole in the presence of plasma: shadow. *Phys. Rev. D*, 92:084005, 2015.
- [44] Tiberiu Harko, Zoltan Kovacs, and Francisco S. N. Lobo. Testing Hořava-Lifshitz gravity using thin accretion disk properties. *Phys. Rev. D*, 80:044021, 2009.
- [45] Songbai Chen and Jiliang Jing. Thin accretion disk around a Kaluza–Klein black hole with squashed horizons. *Phys. Lett. B*, 704:641–645, 2011.
- [46] Cheng Liu, Sen Yang, Qiang Wu, and Tao Zhu. Thin accretion disk onto slowly rotating black holes in Einstein-Æther theory. *JCAP*, 02(02):034, 2022.
- [47] Mohaddese Heydari-Fard, Malihe Heydari-Fard, and Hamid Reza Sepangi. Thin accretion disks around rotating black holes in 4D Einstein–Gauss–Bonnet gravity. *Eur. Phys. J. C*, 81(5):473, 2021.
- [48] Songbai Chen and Jiliang Jing. Properties of a thin accretion disk around a rotating non-Kerr black hole. *Phys. Lett. B*, 711:81–87, 2012.
- [49] Sobhan Kazempour, Yuan-Chuan Zou, and Amin Rezaei Akbarieh. Analysis of accretion disk around a black hole in dRGT massive gravity. *Eur. Phys. J. C*, 82(3):190, 2022.
- [50] Galin Gyulchev, Petya Nedkova, Tsvetan Vetsov, and Stoytcho Yazadjiev. Image of the thin accretion disk around compact objects in the Einstein–Gauss–Bonnet gravity. *Eur. Phys. J. C*, 81(10):885, 2021.
- [51] Cheng Liu, Tao Zhu, and Qiang Wu. Thin Accretion Disk around a four-dimensional Einstein-Gauss-Bonnet Black Hole. *Chin. Phys. C*, 45(1):015105, 2021.
- [52] C. S. J. Pun, Z. Kovacs, and T. Harko. Thin accretion disks onto brane world black holes. *Phys. Rev. D*, 78:084015, 2008.
- [53] Zelin Zhang, Songbai Chen, Xin Qin, and Jiliang Jing. Polarized image of a Schwarzschild black hole with a thin accretion disk as photon couples to Weyl tensor. *Eur. Phys. J. C*, 81(11):991, 2021.
- [54] Marek Rogatko. Positivity of energy in Einstein-Maxwell axion dilaton gravity. *Class. Quant. Grav.*, 19:5063–5072, 2002.
- [55] Ashoke Sen. Rotating charged black hole solution in heterotic string theory. *Phys. Rev. Lett.*, 69:1006–1009, 1992.
- [56] Haiyuan Feng, Yingdong Wu, Rong-Jia Yang, and Leonardo Modesto. Choked accretion onto Kerr-Sen black holes in Einstein-Maxwell-dilaton-axion gravity. *Phys. Rev. D*, 109(6):063014,

- 2024.
- [57] Riccardo Catena and Jan Moller. Axion-dilaton cosmology and dark energy. *JCAP*, 03:012, 2008.
 - [58] Julian Sonner and Paul K. Townsend. Recurrent acceleration in dilaton-axion cosmology. *Phys. Rev. D*, 74:103508, 2006.
 - [59] Indrani Banerjee, Bhaswati Mandal, and Soumitra SenGupta. Implications of Einstein–Maxwell dilaton–axion gravity from the black hole continuum spectrum. *Mon. Not. Roy. Astron. Soc.*, 500(1):481–492, 2020.
 - [60] Siddharth Kumar Sahoo, Neeraj Yadav, and Indrani Banerjee. Imprints of Einstein-Maxwell dilaton-axion gravity in the observed shadows of Sgr A* and M87*. 5 2023.
 - [61] Rebeca Fernández Fernández, Riccardo Della Monica, and Ivan de Martino. Constraining an Einstein-Maxwell-dilaton-axion black hole at the Galactic Center with the orbit of the S2 star. *JCAP*, 08:039, 2023.
 - [62] Bruce A. Campbell, Nemanja Kaloper, Richard Madden, and Keith A. Olive. Physical properties of four-dimensional superstring gravity black hole solutions. *Nucl. Phys. B*, 399:137–168, 1993.
 - [63] David Garfinkle, Gary T. Horowitz, and Andrew Strominger. Charged black holes in string theory. *Phys. Rev. D*, 43:3140, 1991. [Erratum: *Phys.Rev.D* 45, 3888 (1992)].
 - [64] I. D. Novikov and K. S. Thorne. Astrophysics and black holes. In *Les Houches Summer School of Theoretical Physics: Black Holes*, pages 343–550, 1973.
 - [65] Z. Kovacs and T. Harko. Can accretion disk properties observationally distinguish black holes from naked singularities? *Phys. Rev. D*, 82:124047, 2010.
 - [66] Lucas G. Collodel, Daniela D. Doneva, and Stoytcho S. Yazadjiev. Circular Orbit Structure and Thin Accretion Disks around Kerr Black Holes with Scalar Hair. *Astrophys. J.*, 910(1):52, 2021.
 - [67] Diego F. Torres. Accretion disc onto a static nonbaryonic compact object. *Nucl. Phys. B*, 626:377–394, 2002.
 - [68] Indrani Banerjee, Bhaswati Mandal, and Soumitra SenGupta. Signatures of einstein-maxwell dilaton-axion gravity from the observed jet power and the radiative efficiency. *Physical Review D*, 103(4), February 2021.
 - [69] S. Kichenassamy and R. A. Krikorian. Relativistic radiation transport in dispersive media.

- Phys. Rev. D*, 32:1866–1870, 1985.
- [70] G. S. Bisnovatyi-Kogan and O. Yu. Tsupko. Gravitational Lensing in Plasmic Medium. *Plasma Phys. Rep.*, 41:562, 2015.
- [71] Xinzhong Er and Shude Mao. Effects of plasma on gravitational lensing. *Mon. Not. Roy. Astron. Soc.*, 437(3):2180–2186, 2014.
- [72] Shao-Wen Wei and Yu-Xiao Liu. Observing the shadow of Einstein-Maxwell-Dilaton-Axion black hole. *JCAP*, 11:063, 2013.
- [73] Soumya Jana and Sayan Kar. Shadows in dyonic Kerr-Sen black holes. *Phys. Rev. D*, 108(4):044008, 2023.
- [74] Sara Dastan, Reza Saffari, and Saheb Soroushfar. Shadow of a Kerr-Sen dilaton-axion Black Hole. 10 2016.
- [75] X. G. Lan and J. Pu. Observing the contour profile of a Kerr-Sen black hole. *Mod. Phys. Lett. A*, 33(17):1850099, 2018.
- [76] Sérgio Vinicius M. C. B. Xavier, Pedro V. P. Cunha, Luís C. B. Crispino, and Carlos A. R. Herdeiro. Shadows of charged rotating black holes: Kerr–Newman versus Kerr–Sen. *Int. J. Mod. Phys. D*, 29(11):2041005, 2020.
- [77] Meng-He Wu, Hong Guo, and Xiao-Mei Kuang. Shadow Cast of Rotating Charged Black Hole with Scalar Q-Hair. *Symmetry*, 14(11):2237, 2022.
- [78] Akhil Uniyal, Reggie C. Pantig, and Ali Övgün. Probing a non-linear electrodynamics black hole with thin accretion disk, shadow, and deflection angle with M87* and Sgr A* from EHT. *Phys. Dark Univ.*, 40:101178, 2023.
- [79] Wenfu Cao, Wenfang Liu, and Wen-Fang Liu. Parameter constraints from shadows of Kerr–Newman-dS black holes with cloud strings and quintessence. *Gen. Rel. Grav.*, 55(10):120, 2023.
- [80] Javier Badía and Ernesto F. Eiroa. Shadows of rotating Einstein-Maxwell-dilaton black holes surrounded by a plasma. *Phys. Rev. D*, 107(12):124028, 2023.
- [81] Kimet Jusufi. Connection Between the Shadow Radius and Quasinormal Modes in Rotating Spacetimes. *Phys. Rev. D*, 101(12):124063, 2020.
- [82] Xing-Hui Feng and H. Lu. On the size of rotating black holes. *Eur. Phys. J. C*, 80(6):551, 2020.
- [83] Sunny Vagnozzi et al. Horizon-scale tests of gravity theories and fundamental physics from the

- Event Horizon Telescope image of Sagittarius A. *Class. Quant. Grav.*, 40(16):165007, 2023.
- [84] Saurabh Kumar, Akhil Uniyal, and Sayan Chakrabarti. Observational signatures of Rotating compact objects in Plasma space–time. *Phys. Dark Univ.*, 44:101472, 2024.
- [85] Saurabh Kumar, Akhil Uniyal, and Sayan Chakrabarti. Shadow and weak gravitational lensing of rotating traversable wormhole in nonhomogeneous plasma spacetime. *Phys. Rev. D*, 109(10):104012, 2024.
- [86] Volker Perlick and Oleg Yu. Tsupko. Light propagation in a plasma on Kerr spacetime: Separation of the Hamilton-Jacobi equation and calculation of the shadow. *Phys. Rev. D*, 95(10):104003, 2017.
- [87] Volker Perlick and Oleg Yu. Tsupko. Light propagation in a plasma on kerr spacetime: Separation of the hamilton-jacobi equation and calculation of the shadow. *Phys. Rev. D*, 95:104003, May 2017.
- [88] Haroldo C. D. Lima Junior, Luís C. B. Crispino, Pedro V. P. Cunha, and Carlos A. R. Herdeiro. Spinning black holes with a separable Hamilton–Jacobi equation from a modified Newman–Janis algorithm. *Eur. Phys. J. C*, 80(11):1036, 2020.
- [89] Barbora Bezdekova, Volker Perlick, and Jiri Bicak. Light propagation in a plasma on an axially symmetric and stationary spacetime: Separability of the Hamilton–Jacobi equation and shadow. *J. Math. Phys.*, 63(9):092501, 2022.
- [90] V. P. Frolov and I. D. Novikov, editors. *Black hole physics: Basic concepts and new developments*. 1998.
- [91] Edward Teo. Spherical Photon Orbits Around a Kerr Black Hole. *Gen. Rel. Grav.*, 35(11):1909–1926, 2003.
- [92] Samuel E. Vazquez and Ernesto P. Esteban. Strong field gravitational lensing by a Kerr black hole. *Nuovo Cim. B*, 119:489–519, 2004.
- [93] Kazunori Akiyama et al. First M87 Event Horizon Telescope Results. VI. The Shadow and Mass of the Central Black Hole. *Astrophys. J. Lett.*, 875(1):L6, 2019.
- [94] Deng Wang. Shaving the Hair of Black Hole with Sagittarius A* from Event Horizon Telescope. 5 2022.
- [95] Xianglong Wu and Xiangdong Zhang. Connections between the Shadow Radius and the Quasinormal Modes of Kerr-Sen Black Hole. *Universe*, 8(11):604, 2022.